Research Article

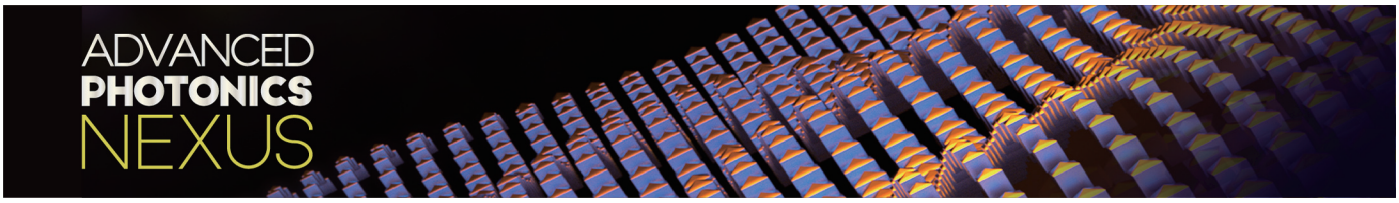

Hybrid optical parametrically oscillating emitter-enabled photoacoustic imaging of water: enhanced contrast, dynamic range, and multifaceted applications

Huajun Tang,[a,†] Yitian Tong,[a,*,†] Mingsheng Li,[a] Najia Sharmin,[a] Jiawei Shi,[a] Bingfeng Li,[b] Chandra Jinata,[a,c] Nikki Pui-Yue Lee,[b] Kevin K. Tsia,[a,c] and Kenneth K. Y. Wong[a,c,*]

[a]The University of Hong Kong, Department of Electrical and Electronic Engineering, Hong Kong, China
[b]The University of Hong Kong, Department of Surgery, Li Ka Shing Faculty of Medicine, Hong Kong, China
[c]Advanced Biomedical Instrumentation Centre, Hong Kong, China

Abstract. Water photoacoustic microscopy (PAM) enables water absorption contrast mapping in deep biological tissue, which further allows a more detailed architecture analysis and facilitates a better understanding of metabolic and pathophysiological pathways. The strongest absorption peak of water in the near-infrared region occurs at 1930 nm, where the first overtone of the O-H bond lies. However, general light sources operating in this band hitherto still suffer from low optical signal-to-noise ratio and suboptimal pulse widths for photoacoustic signal generation. These lead to not only PAM contrast deterioration but also a high risk of sample photodamage. Consequently, we developed a hybrid optical parametrically-oscillating emitter (HOPE) source for an improved water PAM image contrast, leading to noninvasive and safer bioimaging applications. Our proposed source generates 1930 nm laser pulses with high spectral purity at a repetition rate of 187.5 kHz. The pulse width is flexibly tunable from 4 to 15 ns, and the maximum pulse energy is 700 nJ with a power stability of 1.79%. Leveraging these advancements, we also demonstrated high-contrast water PAM in multifaceted application scenarios, including tracking the dynamic of water distribution in a zebrafish embryo, visualizing the water content of a murine tumor xenograft, and mapping the fluid distribution in an edema mouse ear model. Finally, we showcased 1750-nm/1930-nm dual-color PAM for quantitative imaging of lipid and water distributions with reduced cross talk and imaging artifacts. Given all these results, we believe that our HOPE source can heighten water PAM's relevance in both biological research and clinical diagnostics.

Keywords: photoacoustic microscopy; water; optical parameter; near-infrared region.

Received Oct. 13, 2023; accepted for publication Jun. 27, 2024; published online Jul. 23, 2024.

[DOI: 10.1117/1.APN.3.4.046013]

1 Introduction

Water is arguably the most important chemical in biological systems.[1,2] Ranging from cells to organelles, water plays a key role in biological regulation pathways on multiple levels. Tracing the water content in biological systems can therefore facilitate understanding of the underlying mechanism of a multitude of physiological and pathological processes.[3–5] Thus, deviation in tissue water content from the norm can be an indication of various pathological conditions, such as the presence of edema or cancer.[6,7] Some advanced imaging modalities have previously been developed to visualize water content with high spatial resolution, such as coherent Raman scattering microscopy,[8] fluorescence lifetime microscopy,[9] and atomic

*Address all correspondence to Yitian Tong, tongyt89@hku.hk; Kenneth K. Y. Wong, kywong@eee.hku.hk

†These authors contributed equally to this work.

force microscopy.[10] However, the limited sensitivity in such modalities still hinders the maximum achievable contrast of water against the background. In addition, their penetration depths are still impeded by severe optical scattering and attenuation in deep tissue, as well as the depth-related limitation posed by the sensors. Therefore, a more reliable imaging modality is still needed to overcome these challenges. Photoacoustic microscopy (PAM) is a hybrid imaging tool that utilizes laser-induced ultrasound to sense the optical absorption.[11–13] It has been widely utilized in determining the distribution and concentration of chromophores in a label-free manner. Certain chromophore corresponds to a specific optical absorption coefficient at different wavelengths and consequently generates various levels of PA signals.[12] PAM can also improve the penetration depth up to several millimeters due to the less ultrasound scattering in tissues while mitigating background artifacts.[14,15] Leveraging these unique advantages, PAM is deemed to be a promising tool to trace water content in highly scattering biological tissues.

Photoacoustic imaging (PAI) of water at short wavelength near-infrared (NIR) was reported to map the water in tissue and monitor edema formation *in vivo*.[6,16] In addition, a method for analyzing water-rich samples via time-domain terahertz PAI has also been demonstrated to show PA spectrum analysis of water and lipids simultaneously.[17] Despite its demonstration, water suffers a low light absorption coefficient at this spectral region, resulting in poor PAI signal-to-noise ratio (SNR), further limiting both the detection sensitivity and deeper tissue exploration. Compared to operating at short wavelength NIR, the optical absorption coefficient of water is much stronger at long wavelength NIR, especially at 1930 nm.[18,19] This wavelength is the first overtone of the O-H bond, where water has the strongest absorption in the NIR region. Consequently, the longer wavelength also yields a higher water PA signal as well as an improved maximum permissible exposure and low tissue scattering, which further facilitates deep-tissue PAI.[14,20,21] Although water naturally has even higher optical absorption at mid-infrared wavelengths (e.g., 3 μm) than at 1930 nm,[22] the chemical imaging at mid-infrared wavelengths undermines its resolution. Ultraviolet PAM to greatly enhance resolution also involves problems of low sensitivity, phototoxicity, and photodamage. Thus, taking both resolution and absorbance into consideration, the 1930 nm absorption band is the most suitable window for water-based PAI. However, due to pulse width requirement (typically 1 to 20 ns) and mutual restriction between pulse energy and average power (usually tens of nanojoules to a few microjoules), general pulsed laser sources are restricted in their capacity in the 1930 nm band. Below is the brief suitability assessment of the three common methods of pulsed laser generation in relation to PAI at 1930 nm.

1. Mode-locked laser (MLL): The output wavelengths of MLLs can be frequency-shifted to 1930 nm by a high nonlinear fiber and amplified by a thulium-based amplifier system.[23,24] However, the first problem is that the pulse width of the MLL is too short from ~fs to ~ps. Such intense laser pulses with high peak powers are detrimental to the biological sample. Another problem is that the excessive repetition frequency of the MLL can lead to high average power to damage samples.

2. Nanosecond laser based on optical parametric oscillators (OPOs): Based on the theory of four-wave mixing,[25] a wideband nanosecond-pulsed laser can be achieved by placing a gain medium to generate the parametric gain inside an optical cavity and pumping it with a pump source.[25–27] The pulse width (several nanoseconds) and pulse energy (up to 1 mJ) of such lasers are suitable for PAI. Nevertheless, as a nonlinear process, the parametric amplification process caused by the four-wave mixing is too inefficient, resulting in a low optical SNR (OSNR) in the idler optical band (target optical band). Meanwhile, an additional optical filter is required to filter out the target wavelength band to prevent stray light from affecting it, which will further deteriorate the OSNR. In general, due to the limitation of the pump source, the repetition rates of the laser sources based on OPO are relatively low—less than 1 kHz, which restricts the application of OPOs in high-speed PAI.[28–30] In contrast, some specially designed OPO lasers with repetition rates up to several gigahertz are not suitable for PAI due to their high average powers.[31]

3. Pulsed quantum cascade laser (QCL): The QCL is a special kind of semiconductor laser that usually emits mid-infrared light. It can also operate at around 2 μm with a high output power of up to several watts and a flexible repetition rate from 1 Hz to 1 MHz.[32] However, due to the limitation of the relaxation oscillation effect, the pulse width of QCL-generated generated pulses is restricted to tens of nanoseconds with a relatively low extinction ratio. Thus, the frequency of PA signals excited by the pulsed QCL is too close to direct-current noise, which deteriorates the SNR and is further detrimental to imaging quality.

To address these issues, we initially implemented a customized hybrid optical parametrically oscillating emitter (HOPE) at 1930 nm to a transmission-mode PAM. This method can image the volumetric water distribution in highly scattering tissue.[33] We also demonstrated its relevance to biological research. Despite its potential, the initial HOPE is still limited by high amplified spontaneous emission (ASE) noise, oscillating threshold, and nonlinear distortion, which greatly depreciates the output spectrum purity. These effects not only destabilize the output pulse in the time domain but also stretch the pulse width out of the suitable region. All these factors reduce the detection sensitivity of the PA signal and ultimately lead to lower image contrast. Increasing power could be a direct solution to improve the contrast, yet the higher exposure power raises the risks of sample damage.

Our goal is to develop a suitable light source generation method that facilitates high contrast, a large dynamic, and high-speed PAI at long wavelength NIR. Recently, we have briefly reported on our new HOPE and some of the preliminary findings.[34] In this paper, we construct a physical model of the hybrid optical parametrically oscillating system and develop the new HOPE system with high performance in detail. By constructing a double loop gain and controlling the loop gain bandwidth in the fiber-based OPO, the new HOPE can generate a narrowband spectrum with a higher OSNR at 1930 nm. The pulse width of the new HOPE is flexible and continuously tunable from 4 to 15 ns for efficient PA signal generation. Meanwhile, the pulse-to-pulse stability can be guaranteed less than 3.1 ps jitter over a long term under 5 ns pulse width. By introducing a long fiber-back cavity, the new HOPE has a high repetition rate of 187.5 kHz for ultrafast PAI. In addition, the max pulse energy of the new HOPE is up to 700 nJ with improved power stability of 1.79% [root mean square (RMS) @187.5 kHz, 2 h], while the maximum average power is up to 130 mW. The above parameters are hardly realized by the

preceding HOPE system. The proposed new HOPE has performance specifications approaching those of commercial laser sources. To evaluate the system for water PAM with high contrast and a large dynamic, we used our new HOPE system to demonstrate high-contrast PA microscopic imaging of water in adipose tissue with an improved imaging depth of 3.2 mm under 100 nJ pulse energy. Deeper detection depth acquisition with lower pulse energy benefits from higher OSNR and more suitable pulse width of the new HOPE. Furthermore, we showcase the PA signal and imaging with the new HOPE on several biological samples under low pulse energies, including the water distribution in zebrafish embryos, orthotopic murine liver cancer tumor xenografts, and drug-induced ear edema in a murine model. Additionally, we apply the dual-color PAI of both muscle and adipose tissue of bovine tissue with the other source operated at 1750 nm. To our knowledge, this is the first report of exploring the negative contrast of water content in improving lipid imaging by the suppressed artificial signal from 1750 nm. Our findings highlight the fact that the high performance of the new HOPE system for water-based PAI not only facilitates higher imaging dynamics and greater penetration depths but also allows for higher imaging speeds. Moreover, the method of pulse generation from HOPE can be readily extended to other specific long wavelengths of NIR for deep-tissue PAM in biological and biomedical systems as well as the PAI of nonbiological substances.

2 Principle of New HOPE and Experimental Setup

2.1 Principle of the New HOPE

Essentially, the new HOPE is founded by the concept of OPO,[33–35] so it can be analyzed using the basic theory of OPO. Traditional pulsed fiber-based OPOs use high-energy pulsed pump light to induce parametric amplification processes in high nonlinear fibers or photonic crystal fibers.[36–38] Under phase-matching conditions, a wide spectrum gain can be obtained at the Stokes band (the idler wave) and anti-Stokes band (the signal wave). The fiber delay line is used to construct a cavity to form a feedback mechanism for the pump light. The parametric oscillation can be reached when the loop gain is large enough to compensate for the loop loss. Thus, for a lower oscillation threshold in the loop, high loop gains, and low loop loss, is essential.

The basic theoretical mechanism of the new HOPE is depicted in Fig. 1. After power amplification, a pulsed seed is used as the pump light for the laser cavity. A high nonlinear fiber

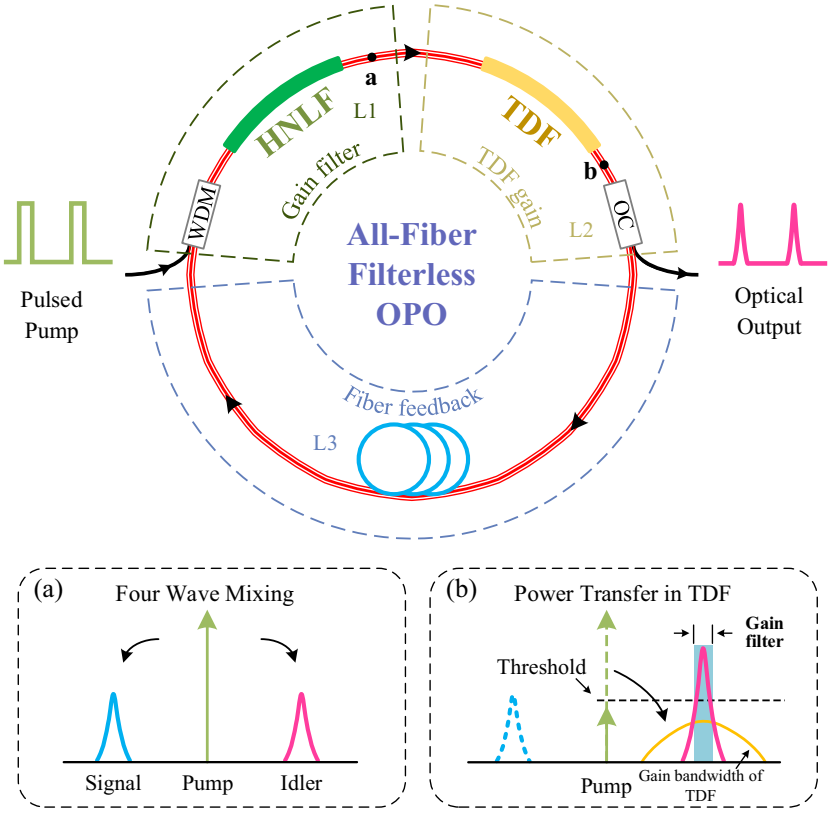

Fig. 1 (a) and (b) The basic theory of the new HOPE. The desired optical pulses are generated in an all-fiber filterless OPO. It includes an HNLF, which provides the parametric gain, a feedback fiber, and a short TDF for gain compensation. The cavity is driven by an optical pulsed pump. The two insets, respectively, represent the gain transformations of points a and b in the OPO, in which the dashed lines show that the indicated signal energy decreases and disappears. WDM, wavelength-division-multiplexer; HNLF, highly nonlinear fiber; TDF, thulium-doped fiber; and OC, optical coupler.

(HNLF; L_1) and a thulium-doped optical fiber (TDF; L_2) are used as twofold optical amplification to provide the cavity gain. A long fiber (L_3) is used as the feedback to form an oscillator loop. Among them, the HNLF provides two roles in the loop, of which one is wavelength transformation. According to the degenerate four-wave mixing, for a given high power pump ω_p, the generation of two sidebands, called signal wave ω_s and idler wave ω_i, and the frequency shift $\Delta\omega$ can be described as

$$\Delta\omega = \omega_p - \omega_i = \omega_s - \omega_p. \tag{1}$$

By tuning the frequency of the pump, we can get the idler wave ω_i wavelength around 1930 nm. That also means that the output wavelength of the new HOPE can be tuned by adjusting the pump wavelength under the premise of ensuring the loop oscillation.

Another role is to provide the parametric gain g, which can be described as[39]

$$g = \sqrt{(\gamma P_{\text{in}})^2 - \left(\frac{\Delta k}{2} + \gamma P_{\text{in}}\right)^2}, \tag{2}$$

where γ is the Kerr nonlinearity coefficient of the HNLF, P_{in} is the input pump peak power, and Δk is the maximum wavefront mismatch. Obviously, the cavity has the max gain when Δk equals $-2\gamma P_{\text{in}}$. The unsaturated gain of the idler wave for each time can be described as

$$G_{\text{idler}} = \left(\frac{\gamma P_{\text{in}}}{g}\right)^2 \sin\, h^2(gL_1). \tag{3}$$

In accordance with the general solution of Eq. (3), the idler gain involves the consumption of a fractional portion of the pump power (typically less than 10%). This process consumes very little pump power. Thus, the residual bulk pump light can be used as a pump for the second-stage gain of TDF. As a result, the total gain of the loop can be described as

$$G_{\text{loop}} = G_{\text{idler}} + g_{\text{TDF}}(P_{\text{in-average}})L_2, \tag{4}$$

where g_{TDF} is the gain of TDF, which is directly proportional to the effective pump average power ($P_{\text{in-average}}$). Hence, in essence, the parametric and the TDF gains complement each other in the loop.

Another important loop parameter is the gain bandwidth, which determines the maximum spectrum bandwidth of the output optical signal of the oscillator. Since TDF has a wide gain bandwidth, the gain bandwidth of the loop is determined by the parametric gain bandwidth. For a short section of HNLF, the parametric gain bandwidth can be written as

$$B_P = \sqrt{\gamma P_{\text{in}}/2|\beta_2|}, \tag{5}$$

where β_2 is the dispersion value of the HNLF. To get a particular wavelength of the idler wave with a certain HNLF, the values of γ and β_2 are predefined. Therefore, the parametric gain bandwidth is determined by the pump power. In addition, the oscillation threshold of the OPO can be expressed as[40]

$$\mu = 2\kappa\sqrt{P_{\text{in}}}L_1/\Lambda_e = 1, \tag{6}$$

$$\Lambda_e = \left(\frac{2|\beta_2|B_P^2}{g}\right)^2 \sin\, h^2(gL_1) + g_{\text{TDF}}L_2 - \Lambda_{\text{intracavity}}, \tag{7}$$

where κ is the effective second-order nonlinearity of the HNLF, Λ_e is effective intracavity loss, and $\Lambda_{\text{intracavity}}$ is the total intracavity loss.

For PAI, we aim to get a high monochromaticity of the idler wave output. In the loop of the new HOPE, the parametric gain forms a gain filter function with a narrow gain bandwidth. When the gain bandwidth is reduced by tuning the gain filter, the optical signals in the desired bandwidth can be satisfied by the loop oscillated condition corresponding to Eq. (7) to achieve the output narrowband spectrum. Thus, the frequency selection can be achieved by controlling the parametric gain bandwidth without additional filters or any other frequency-selective devices.

Different from the traditional optical parametric amplifier, the low-duty cycle of the pump wave will result in high ASE noise from the TDF gain. Further, the ASE noise will be output with the signal wave if the gain of ASE noise is higher than the loop loss. Therefore, to decrease the ASE noise of the output, the average power of the pump ($P_{\text{in-average}}$) needs to be increased by decreasing the modulation depth of the pump wave. Hence, the new HOPE loop can keep stable oscillation with narrow loop gain bandwidth for the high monochromaticity output without ultrahigh pump power.

2.2 Experimental Setup

The HOPE system and PAM are schematically depicted in Fig. 2. An electro-absorption modulated laser (EML) with a center wavelength of around 1550 nm is employed to generate an optical pulsed pump. The EML can achieve high-speed modulation driven directly by an electrical pulse signal generated from a function generator. Thus, a series of rectangle optical pulses with a flexible extinction ratio can be simply obtained, of which the optical pulses have a pulse width of 5 ns with a rise/fall edge of 1 ns. Then the pulsed pump is amplified by a cascaded optical amplifier including a low noise erbium-doped fiber amplifier (EDFA) and a medium-power EDFA. After being amplified, the seed signal is fed into the fiber-based OPO cavity via a polarization-maintaining 1550/1930 nm wavelength-division-multiplexer (PM-WDM). The common port of the PM-WDM is fed into a polarization controller (PC) to adjust the linear polarization state. After the PC, the pump signal is fed into a spool of 50 m highly nonlinear fiber to perform four-wave mixing, and then empirically cascaded with a 0.8 m long TDF (TmDF200, OFS). The HNLF and TDF are used to achieve parametric amplification and auxiliary optical amplification. After the TDF, the desired idler signal is output by a 50:50 coupler. The residual pump power is feedback to the loop again through a 1 km PM fiber coil. More details are discussed in the Supplementary Material. A tunable delay line is inserted into the feedback to enable fine-tuning of the fundamental cavity repetition rate. Thanks to the long feedback, the new HOPE has a stable pulse output with a repetition rate of 187.5 kHz. In addition, a fiber circulator (CIR) with a light trap is placed before the HNLF to extract the reflected light. Finally, a thulium-doped fiber amplifier (TDFA) is applied to amplify the output of the OPO cavity to 130 mW as well as absorb the residual pump. To facilitate measurement and monitoring, a 90:10 coupler @1930 nm is inserted after the TDFA,

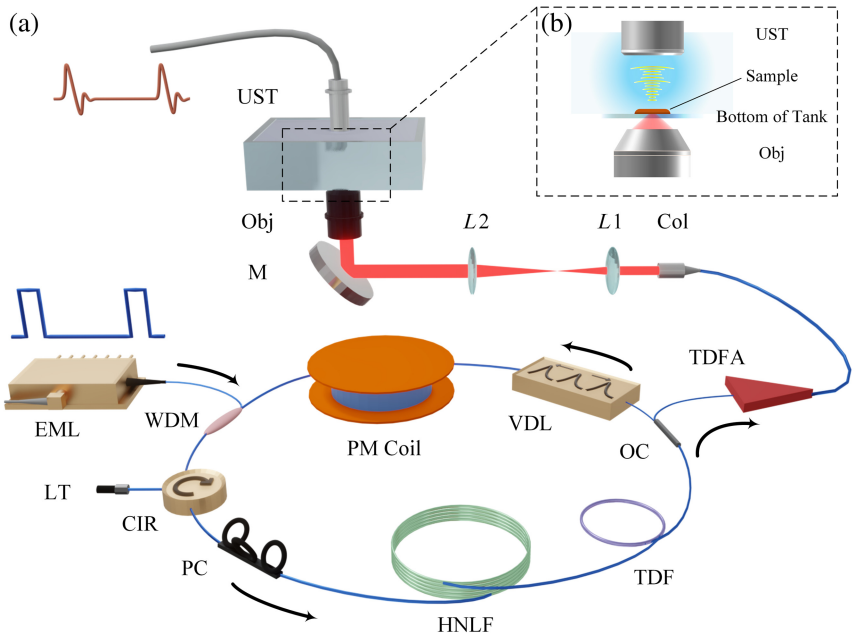

Fig. 2 (a) and (b) Schematic representation of HOPE system and PA microscope. EML, electro-absorption modulated laser; WDM, wavelength-division-multiplexer; CIR, circulator; LT, light trap; PC, polarization controller; HNLF, highly nonlinear fiber; TDF, thulium-doped fiber; OC, optical coupler; VDL, variable delay line; PM coil, 1-km polarization-maintaining fiber core; TDFA, thulium-doped fiber amplifier; Col, collimator; *L*1, $f = 75$ mm lens; *L*2, $f = 150$ mm lens; M, mirror; Obj, microscope objective lens; and UST, ultrasound transducer.

where the 90% part is used for imaging and the 10% part is utilized for monitoring.

For the PAM part, the HOPE's output is collimated into free space by a collimator and sent to a home-built PA microscope. After being expended by a $4f$ system to match the objective's back aperture, the beam is focused by the objective (M-10X, Newport) to illuminate the sample in a water tank. The tank is installed on an X-Y 2D linear stage (MT-85, MICOS) for raster scanning. To avoid the influence of background noise, heavy water is used as the ultrasonic coupling medium in lieu of regular water in the water tank, as heavy water has the same chemical properties and elastomeric coefficient as ordinary water. The PA signal from the sample is detected by an ultrasound transducer (V311-SU, Olympus NDT) positioned right above and converted to the electrical signal, as shown in Fig. 2(b). The signal is then amplified by a 28.5 dB radio frequency (RF) amplifier (ZFL-500LN+, Mini-Circuits) and filtered by a 20 MHz lowpass filter cascaded with a 750 kHz high-pass filter. After that, the electrical signal is sampled and sent to the computer by a real-time oscilloscope (SDA8Zi-B, Teledyne LeCroy) for analysis.

3 Result

3.1 Characterization of the New HOPE

The performance of the new HOPE is characterized in the frequency domain and time domain, as shown, respectively, in Fig. 3. First, the output optical spectrum of the new HOPE from the monitoring terminal is measured by an optical spectrometer in the frequency domain. With the increase of frequency difference between the central wavelength of the EML and the zero-dispersion wavelength of the HNLF, the output wavelength of the new HOPE is redshifted. Nte that the new HOPE source enables continuous wavelength variation from 1943 to 1916 nm by tuning the center wavelengths of the EML from 1550 to 1552 nm. These optical spectrums with partial center frequencies are shown in Fig. 3(a). The difference in spectral amplitude is mainly due to the gain bandwidth and gain flatness of the TDF. The measured optical spectrum centered at 1930 nm has a 0.25 nm spectral bandwidth at −3 dB and around 2.83 nm spectral bandwidth at −50 dB. Such a sharp peak proves that the new HOPE has a highly monochromatic spectrum with low noise and high OSNR, thanks to pump power regulation with dual-loop gain. Therefore, the new HOPE can provide highly effective power with precise tunability over a wide range, which reduces the overall power required to excite the PA signal.

In the time domain, the optical pulses generated by the new HOPE are characterized by a high-speed photodiode at the monitor part. Before being fed into the photodiode, an optical attenuator of 20 dB is added to protect the photodiode from power saturation or even damage from the high peak power. Thus, a total of 30 dB optical attenuation is applied for measurement in the time domain, including 10 dB attenuation introduced by a 90/10 optical coupler. The output of the photodiode is recorded by a high-speed real-time oscilloscope (MSOX 6004A, Keysight). The recorded pulse train over a 200 μs duration and the inset zoom in the single pulse are shown in Figs. 3(b) and 3(c), respectively. By matching the repetition rate to the intrinsic cavity length, we get stable laser pulses with a pulse width of 5 ns and a repetition rate of 187.5 kHz. It can be seen that the SNR in the time domain is comparatively high up to about 0.8 $V_{p\text{-}p}$ under 30 dB optical attenuation, standard 50 Ω transimpedance of the photodiode, and no RF amplification. This also

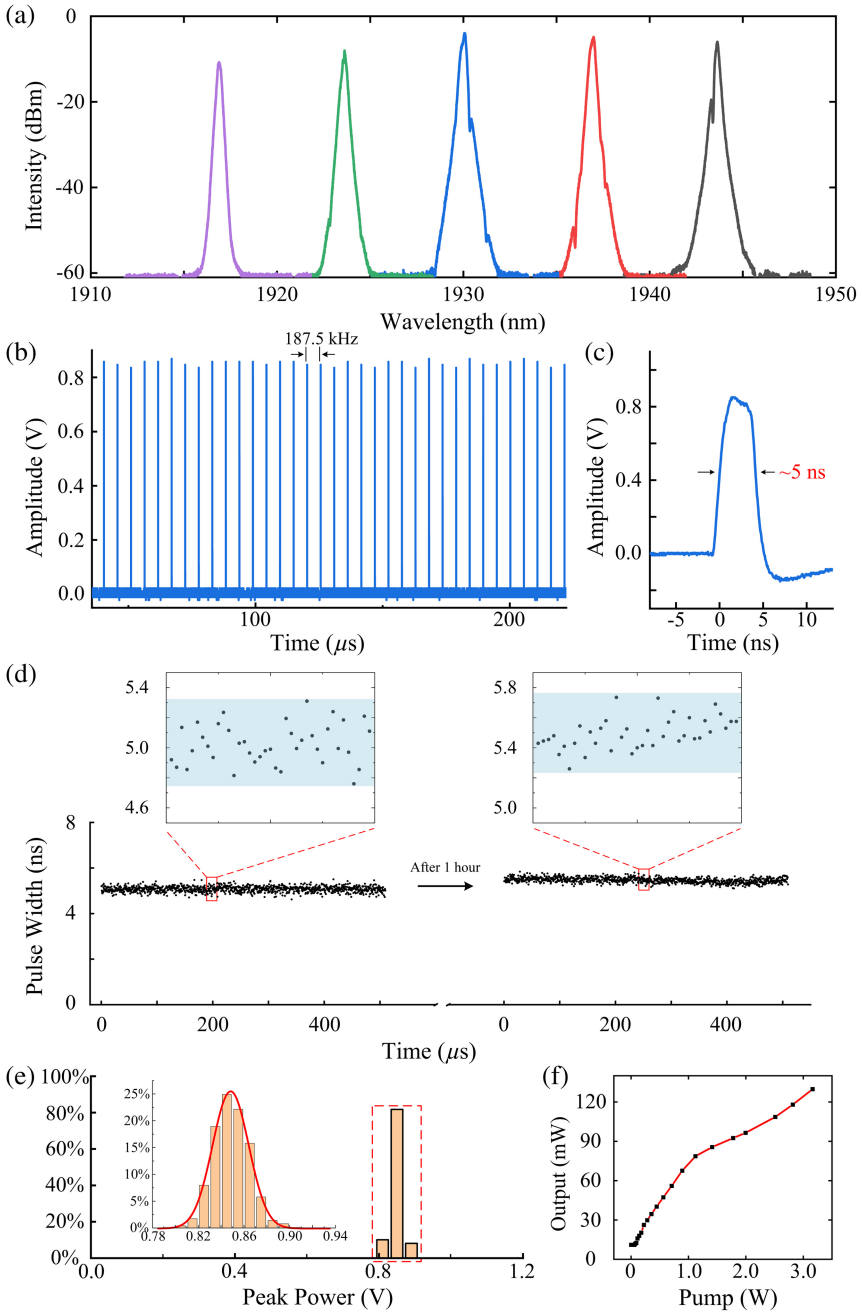

Fig. 3 Characterization of the new HOPE's output. (a) Output spectrum of the new HOPE. (b) Time trace of the new HOPE's output. (c) Zoomed-in single pulse of (b). (d) Pulse-to-pulse widths of the new HOPE's output at the start and after 1 h. (e) Pulse intensity histogram. (f) The relationship between the output power of the new HOPE and the pump power of TDFA.

indicates that the output of the new HOPE has a high OSNR. In addition, due to the precise matching of the loop delay, the generated pulse can maintain stable oscillation within a certain range. Just by tuning the function generator's delivering pulse width to the EML, the new HOPE's pulse width can be continuously tuned from 4 to 15 ns without any hardware replacement. More details are shown in the Supplementary Material.

Furthermore, the long-term stability of the new HOPE is also verified. To this end, pulse-to-pulse width variation over an extended time period is recorded and measured. Due to the extremely low duty cycle of the pulse signal, 1000 individual pulses are sampled continuously with a high sampling rate by successive single triggers to obtain higher sampling accuracy, instead of sampling the restricted 1000 pulse sequence once. The pulse width of each pulse is calculated, respectively, and shown in Fig. 3(d). From the result, the pulse width of the generated pulses from the new HOPE is kept to 5 ns with a pulse-to-pulse time jitter of 2.7 ps. After 1 h, another 1000 signal pulses are resampled and calculated, and the result is shown in Fig. 3(d) as well. The pulse width mildly deteriorates by 7% to 5.352 ns,

and the pulse width jitter deteriorates by 14.8% to 3.1 ps. This slight deterioration is caused by the jitter accumulation of loop delay caused by ambient temperature changes.

Meanwhile, we characterize the stability of the new HOPE's power output as well. The above 2000 pulses are calculated for the pulse intensity histogram shown in Fig. 3(e). The pulse amplitude is mainly concentrated around 0.85 V, and rarely below 0.7 V or above 0.9 V. That is, the pulse energy fluctuation rarely exceeds 6%. The ratio of standard deviation to the mean (std/mean) is calculated to be 1.79%. The power stability is greatly enhanced by the low time jitter of the system. This is because the high stability in the time domain ensures the stability of resonant amplification in the OPO cavity. As a result, the long-term stability of both power and pulse width confirms the reliability of long-time imaging and multiple signals averaging results. Thus, the new HOPE system can provide a stable pulse width and power in pulse-to-pulse, which is significant for long-time PAI, multiple signal accumulation, etc. After that, we measure the new HOPE's output power by an integrating sphere photodiode power meter. By tuning the pump power of the TDFA, the output power concerning the pump power is shown in Fig. 3(f). Linear fits data show that the HOPE system output power increases almost linearly with the pump power.

3.2 PAI for Water via the New HOPE

In the next step, the capability of the new HOPE system in imaging the water content within tissues is verified. The evaluation of the imaging performance is based primarily on two metrics: the SNR of the PA transients in water, and the contrast achieved in the water against other components. First, the SNR of the water-based PA signal was obtained by stimulating a transient in pure water, the results of which are shown in Fig. 4(a).

It must be noted that there was significant component loss along the path of propagation of the new HOPE emission, mainly because the objective lens used in the system was not specialized for the NIR band. After an attenuation of around 5 dB, the pulse energy exciting the PA signal was approximately 24 nJ (corresponding to 80 nJ emission pulse energy). It was found that this excited an SNR of 20 dB without any averaging. This can be compared to our previous work with the 1930-nm HOPE, which achieved an SNR of 19 dB at 300 nJ and an average of 4 times (corresponding to 13 dB without any averaging). Thus, the new HOPE achieves a remarkable SNR improvement with only 8% of the pulse energy, demonstrating the suitability of the source for PAM even at ultralow pulse energies. This superiority is due to the improved performance of the new HOPE in terms of its high OSNR and pulse duration of 5 ns being more suited to PAI. This also indicates that the new HOPE has higher PA excitation efficiency to improve the dynamic range of the system under fixed detection conditions. The corresponding FFT spectrum to the water signal and its Gaussian fitting curve is shown in Fig. 4(b) in which the central frequency of the water signal is shown as around 7 MHz and the spectrum bandwidth of the signal is about 8 MHz @ 3 dB.

Considering lipid is one of the most widely distributed constituents of biological systems, the ability of the new HOPE to achieve sufficient distinction between lipid and water is also investigated to verify that the absorption of lipid in the 1930-nm window does not deteriorate the contrast between the two components. To this end, PA signals are generated in water and butter, as shown in Figs. 5(a) and 5(b).

The excitation energy on the sample is set at 24 nJ on the sample. The PA signal of water is found to be 34 times higher in amplitude than the signal generated in butter under the same excitation pulse energy. Thus, even at ultralow pulse energies, a high positive contrast of water against lipids can be achieved. Such a capability is further utilized for imaging the muscle distribution in a specimen of bovine tissue at 1930 nm, as shown in Fig. 5(c). The black dashed box encloses the area imaged in the experiment, and the results are presented in Fig. 5(d). Comparing the two images visually, it can be deduced that the distribution of the PA signal amplitude corresponds closely to the distribution of the muscle and the adipose tissue within the sample. For instance, the adipose tissue lies within the region bounded by the yellow dashed line in Fig. 5(c). This structure appears as a dark region within the PA image, and the structural components have been visualized. Given that this imaging was carried out with low pulse energy at the site of excitation, this is a much lower pulse energy than the previously reported implementation of the 1930-nm HOPE. This is owing to the far superior OSNR of the emission spectrum of the new HOPE, which was facilitated by the elimination of ASE noise and continuous-wave signals in the output spectrum. Furthermore, enhancement in the long-term stability of the new HOPE is also a contributing factor to the imaging performance at ultralow pulse energies. The maintenance of the pulse width at a constant value over the imaging period prevents deterioration of the PA signals produced over time and ensures a higher quality of the imaging parameters.

Utilizing the contrast of muscle and adipose tissue, depth imaging through the application of the new HOPE is also realized. Figure 6(a) shows the thick section of the bovine tissue that was used for this purpose. The excitation energy is increased to

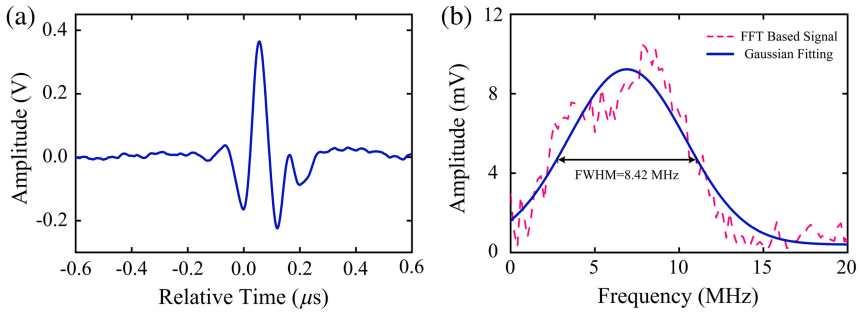

Fig. 4 (a) PA signal of water obtained at 1930 nm and its frequency spectrum with Gaussian fitting. (b) FFT spectrum of PA signal and its Gaussian fitting result.

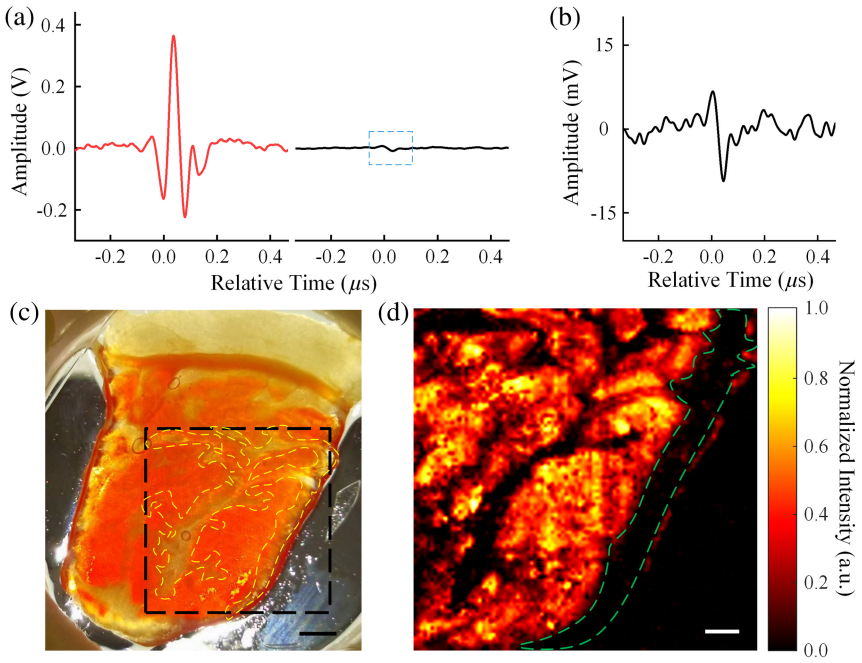

Fig. 5 (a) PA signal of water (red) and butter (black) obtained at 1930 nm. (b) Zoomed-in signal of butter in panel (a). (c) Photograph of the sample and the imaging region. The black dashed box encloses the area imaged in the experiment, in which the adipose tissue lies within the region bounded by the yellow dashed line (scale bar: 2 mm). (d) PAI of the water content at 1930 nm (scale bar: 1 mm; image acquisition time: ~40 min). The region bound by the green dotted line denotes adipose tissue.

about 100 nJ on the sample. The 3D rendering view image in Fig. 6(b) shows the surface of muscle through adipose tissue that is at least 1 mm thick. The B-mode image in Fig. 6(c) shows the muscle surface pattern at a depth of more than 3.2 mm above the adipose tissue. In Fig. 6(c), there are some bright spots below the top layer, which could be contributed by blood vessels with rich water content. The z axis in the two images is from the bottom to the top, opposite the real direction of illuminating of the bovine tissue. This is consistent with the orientation of the imaging system, as shown in Fig. 2(b). This high penetration

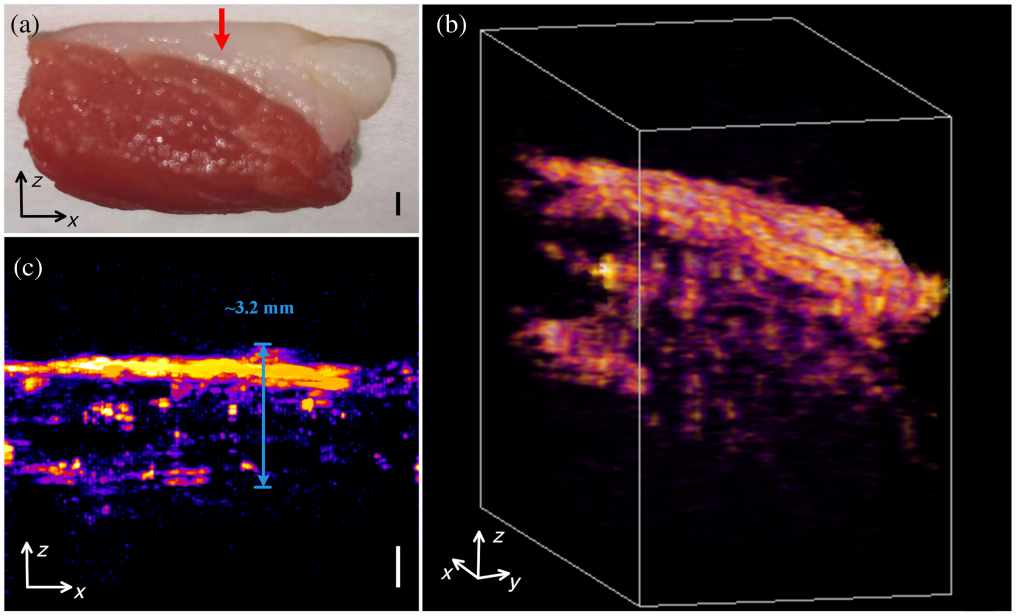

Fig. 6 (a) Photograph of the sample and indication of the illuminating direction. (b) 3D PA image of muscle surface with image acquisition time: ~40 min. (c) B-mode image of (b). (Scale bar: 1 mm.)

depth benefits greatly from not only less photon scattering in biological tissues at 1930 nm but also the high OSNR of the laser pulse from the new HOPE. Meanwhile, the improved imaging depth of 3.2 mm under just 100 nJ pulse energy in the adipose tissue is another piece of evidence of the system's high dynamic range.

3.3 Water PAI Applications in Biological Samples

The use of bond-selective imaging modalities to image target biomolecules within the zebrafish anatomy can open the door to *in vitro* studies to visualize the evolution of specific tissue chromophores. Moreover, the understanding of the anatomical structure of the zebrafish embryo can be furthered by imaging the distribution of the most prevalent tissue components, such as lipids, proteins, and water. Previously, Høgset et al. demonstrated whole-body imaging of the zebrafish through confocal Raman spectroscopy combined with multivariate analysis, interrogating tissue components including proteins, lipids, carotenoids, and DNA.[41] However, to the best of our knowledge, hitherto there has been no report showcasing water distribution in zebrafish, which could be important for teleost fish embryo cryopreservation.[42,43] Hence, this gap was addressed by employing the newly developed PAM system based on the 1.9 μm new HOPE. The experiment was carried out by fixing a zebrafish embryo 48 h postfertilization and imaging its water composition at 24-h intervals with an image acquisition time of ~30 min, as depicted in Fig. 7. The excitation energy is set at about 20 nJ on the sample.

The whole-embryo images taken at 0, 24, and 48 h followed by fixation of the 48 h postfertilization (hpf) zebrafish illustrate a noticeable water distribution dynamic in the embryo. Immediately after fixation, the zebrafish embryo shows a substantial distribution of water over its body. The water is most concentrated in the tail region and the edge of the yolk sac, as shown in Fig. 7(b). After 24 h of fixation, the water distribution shows a visible decline as the water diffuses out due to the loss of regulatory metabolic functions in the organism. It is worth observing that the water concentration at the periphery of the embryo decreases most significantly, with the tail region showing the highest loss in its water content due to the permeability of the epidermis from the results in Fig. 7(c). At the end of the 48-h mark in Fig. 7(d), the yolk sac retains some of its water content. In contrast, the water content over the rest of the embryo has diffused out. With these dynamic observations, utilizing our new HOPE water-imaging system, a water map distribution of the 48 hpf zebrafish embryo was demonstrated for the first time. The marked changes in the water concentration at progressive time intervals validated the performance of the new HOPE imaging system in tracing the changes in the water content of the embryo.

Other than that, visualization of certain biomarkers of cancerous tissues can facilitate the detection of their presence. This effort can subsequently augment the existing understanding of their progression pathways and, more importantly, provide insights into plausible treatment options. Cancers are marked through the presence of certain biochemical compounds, the so-called biomarkers, which signal the presence and the stage of the disease.[44] To address this direction, a label-free and bond-selective imaging system, such as PAM, can play an indispensable role in identifying and tracing such cancerous biomarkers without altering or destroying the tissue sample.

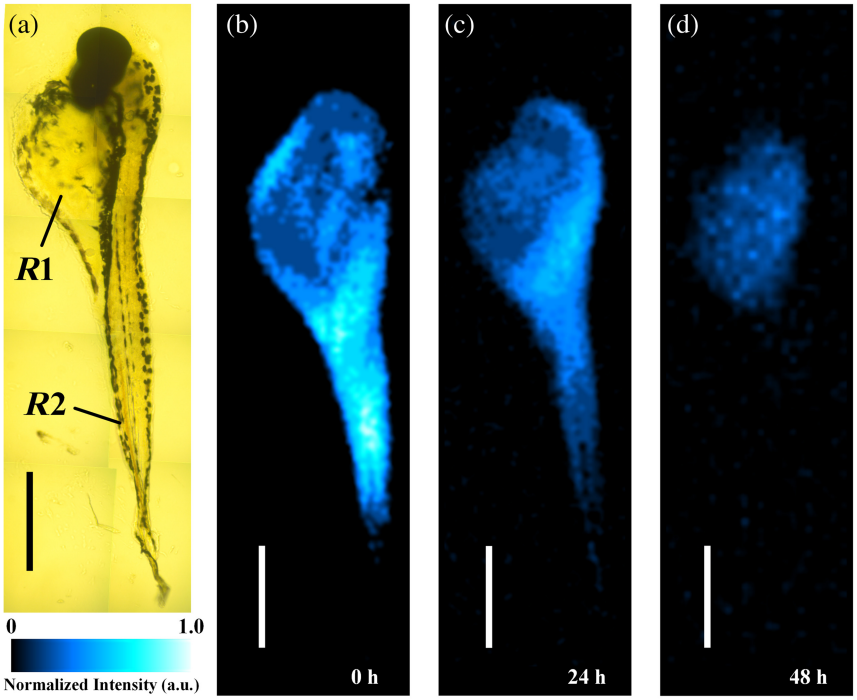

Fig. 7 (a) Photograph of the zebrafish embryos, where region *R*1 is the yolk sac and *R*2 is the tail. (b) The water PAI of the zebrafish embryos with image acquisition time: ~30 min. (c) The water PAI of the zebrafish embryos after 24 h. (d) The water PAI of the zebrafish embryos after 48 h with image acquisition time: ~30 min. (Scale bar: 500 μm.)

A previous study by Penet et al. found a significant discrepancy in the water content between a normal and cancerous pancreas.[45] However, the role of water in differentiating between cancerous structures as opposed to healthy tissues remains relatively underexplored. Supplementing current diagnosis protocols and biopsy techniques with water imaging can potentially provide extra information about the morphological features of liver cancer lesions, which may further aid more effective diagnosis and treatment.[46,47] Hence, the PAM for water in a cancerous liver xenograft sample was illustrated using the proposed new HOPE system in this study. An orthotopic mouse xenograft model of liver cancer was employed for this purpose. A 1 cm × 1 cm section of the liver cancer xenograft was imaged to obtain its water PAM, as shown in Fig. 8. The excitation energy is set at about 40 nJ on the sample.

The cancerous liver tissue spans the edge of the sample, with the inner sections being healthy tissue. The results of the water imaging are consistent with this fact, as the highest concentration of water is seen around the edges of the sample. The boundary of the sample in the lower right-hand side of the PA image in Fig. 8(b) can also be visualized and agrees with the photographed sample in Fig. 8(a). Despite this observation, the section of the PA image delineated in yellow marks an experimental error, as the sample was not flat on the optical window of the PAI chamber. Consequently, the excitation beam was not incident on the sample, and any PA signals could not be collected in this segment. Nevertheless, this preliminary study demonstrated the potential of the new HOPE in highlighting water distribution in a small sample of cancerous liver tumors. We expect that the imaging system can further advance for oncology diagnostics and therapy.

Another pathological condition that is highly characterized by excessive water level within tissues is edema: swelling resulting from a buildup of fluids in the interstitial space within tissues.[47] Given its associations with the inflammatory response, edema can arise from trauma, infection, and/or metabolic disorders, either at a localized or systemic level.[47,48] Research into inflammation pathways, mechanisms of edema formation, and effectiveness of anti-inflammatory drugs have largely been conducted through mouse edema models.[49,50] However, detailed edema imaging in a mouse ear model has not yet been reported. Employing the new HOPE-based PAM system developed in this study, the visualization of the water distribution within a mouse ear edema is demonstrated for the first time.

In this *ex vivo* study, the edema was induced in one ear of a mouse using dimethylbenzene. The other ear from the mouse was left intact as a control. The ears from the mouse were excised from the mouse and imaged separately with the new HOPE PAM setup under strictly the same pulse energy of 50 nJ. Figures 9(a) and 9(b), respectively, illustrate the water distribution in the normal and the edematous ear with normalized intensities, while Figs. 9(d) and 9(e) illustrate the corresponding imaging depths being encoded using the color scale. In line with expectations, the ear with the edema shows a much stronger PA signal over most of the scanned area compared to the normal ear. This is in line with the fact that the edema formation is driven by an accumulation of water-containing fluid in the tissue. To intuitively illustrate that the ear with the edema has a stronger PA signal, Fig. 9(c) gives the corresponding PA amplitudes along the axial yellow line [Figs. 9(a) and 9(b)] passing through approximately the same structures in the two ears, respectively. The capacity of the new HOPE PAM system also allows the variation in the concentration of fluid within the edema to be pictured. From Fig. 9(b), it can be seen that the PA signals are generally the most intense at the helix of the edema ear. This implies that this section of the ear experienced the highest level of fluid accumulation, which is likely the indication of a stronger localized inflammatory response. Near the lower right corner of Fig. 9(b), the region labeled *R*2 shows low signal intensities. This corresponds to the presence of cartilage tissue in the ear, which is also apparently in the normal ear in the region marked *R*1 in Fig. 9(a). Hence, the results of this *ex vivo* experiment highlight that the new HOPE-based PAM system can effectively utilize the intrinsic water contrast of tissues to not only differentiate edematous structures from normal tissue but also offer sufficient sensitivity to distinguish structural details within the edema region itself.

3.4 Dual-color PAI of the Water and Lipid Distribution

Water and lipids are among the most important chemicals in the biological system. Therefore, high-resolution imaging of both contents could be vital in deciphering various biological metabolic mechanisms. Abnormal concentration of water and lipids

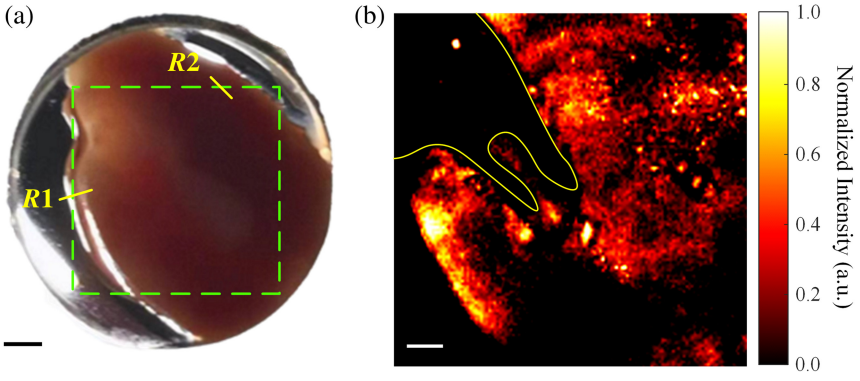

Fig. 8 (a) Orthotopic mouse liver tumor xenograft sample in which the green dashed line box represents the imaging region (scale bar: 2 mm, region *R*1: tumor tissue; and region *R*2: healthy tissue). (b) PA water image of liver cancer sample with image acquisition time: ~30 min. (Scale bar: 1 mm.)

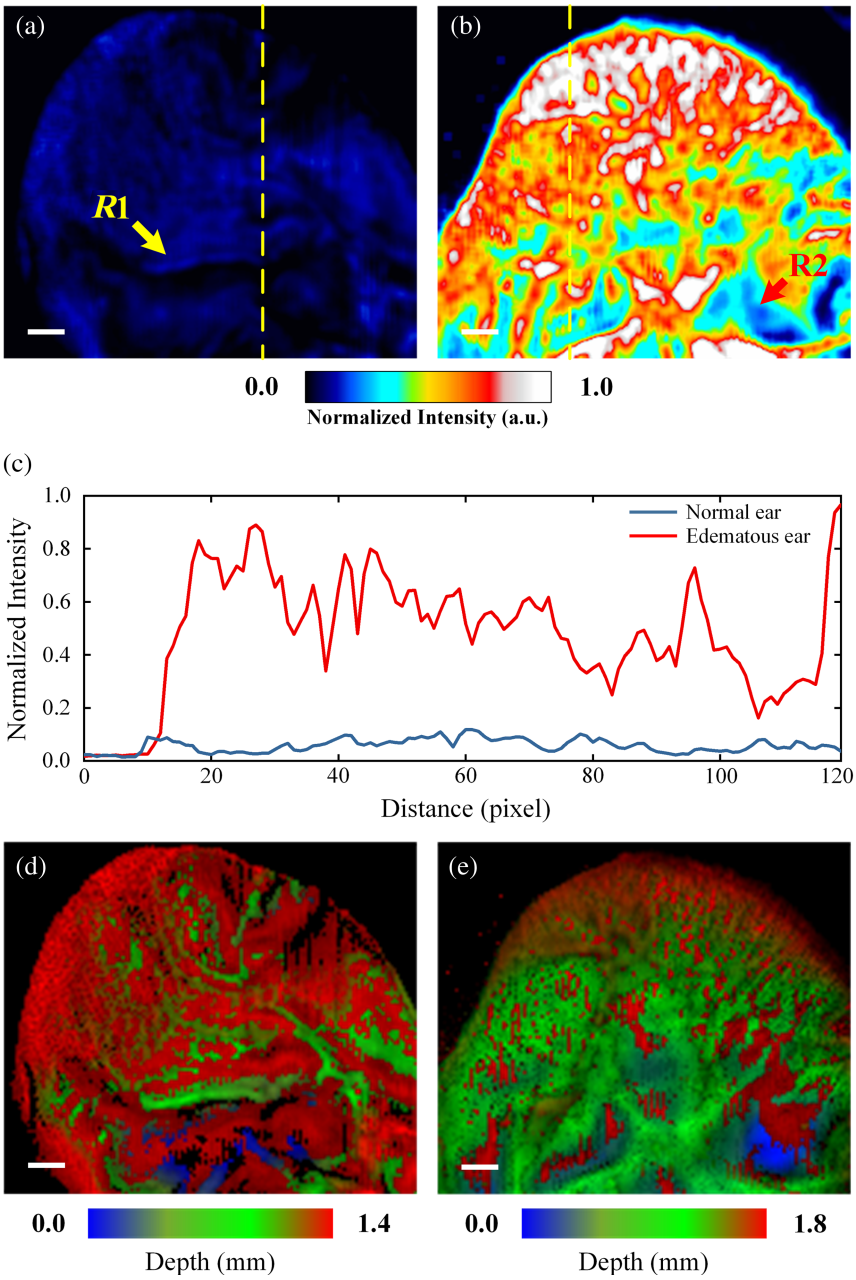

Fig. 9 PAI of water distribution in the ear with normalized intensities with image acquisition time: ~40 min. (a) The water PAI for a mouse normal ear. (b) The water PAI for the ear of a mouse with edema, where the presence of cartilage is marked *R*1 and *R*2. (c) PA amplitude values corresponding to the axial yellow lines passing through approximately the same structures in the left and right ears in (a) and (b), respectively. (d) and (e) Depth-encoded maximum amplitude projection images corresponding to (a) and (b), respectively. (Scale bar: 1 mm.)

is closely related to many diseases, such as inflammatory disorders, diabetes, and cardiovascular disease. Previously, functional magnetic resonance imaging (fMRI), hyperspectral optical imaging, and coherent Raman scattering (CRS) microscopy were the prime approaches to generate water and lipid contrast. However, fMRI lacks chemical specificity and suffers from poor spatial resolution. Hyperspectral optical imaging is still inadequate in circumventing the severe optical scattering in the tissue, which further limits its penetration depth and requires a complex algorithm to compensate for its local fluence fluctuations. CRS microscopy suffers from the limited cross-section area and severe scattering in the tissue. PAI has been well demonstrated to visualize the lipids and water in the cardiovascular, skin, brain, and other organs.[6,51,52] At the shortwave-infrared regions of 1.7 and 1.9 μm, water and lipid both have a strong absorption characteristic due to the overtone vibrational absorptions.[30] Therefore, PAI of both chromophores in this region has inevitable cross talk, and it cannot accurately reveal the content of each chromophore. Here, we employed our new HOPE laser and previously developed 1.7-μm pulse laser to

image the lipid and water in the same field of view. Our dual-color PAI system at short-wavelength NIR can suppress the imaging artifacts and avoid the cross talk in the PAI of water and lipids. This allows quantitative PAI of the water and lipid content.

Meanwhile, according to the previous experiment, the water content imaging shows an interference signal from lipid or adipose tissue. A home-built laser source emitting at 1750 nm[53] is combined with the new HOPE for imaging lipid and water content in the same field of view. The pulse energies of the new HOPE and 1750-nm laser are set at 60 and 300 nJ. A 1-mm-thick bovine tissue is immersed in heavy water to minimize the interference signal, and the region in the yellow dashed box in Fig. 10(c) is imaged. The benefit of placing the sample in heavy water is twofold: first, heavy water can be used as a good ultrasound coupling medium, just like ordinary water; second, heavy water avoids generating any interfering signals for PAI of water and lipids. It is observed that the imaging of water and lipids shown in Figs. 10(a) and 10(b) roughly match the distribution of muscle and adipose tissue in the specimen. It can be noted that the water-based PAI shows a higher level of detail. This goes to show that the 1930-nm new HOPE

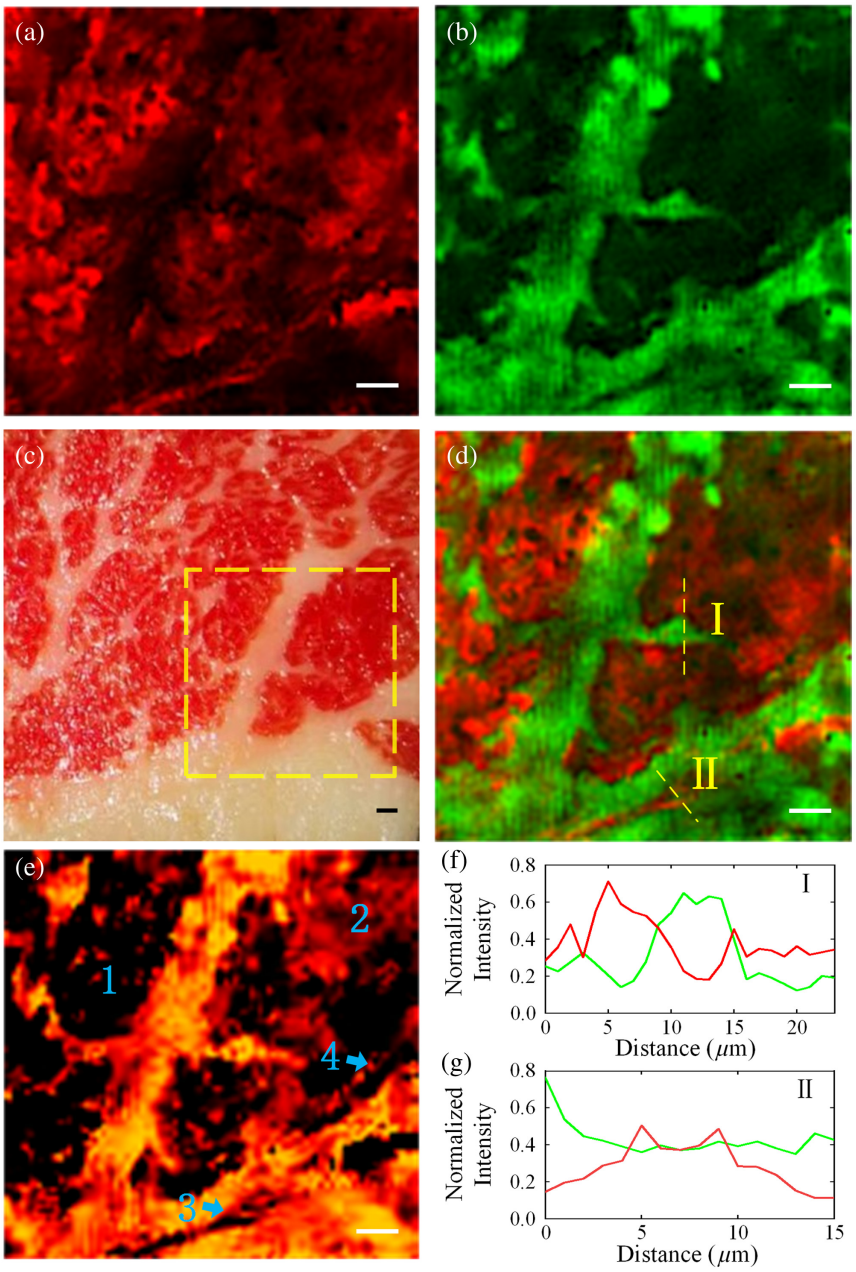

Fig. 10 (a) PAI of water content acquired at 1930 nm with image acquisition time: ~40 min. (b) PAI of lipid acquired at 1750 nm with image acquisition time: ~55 min. (c) Photograph of the sample, where the yellow dashed line box represents the imaging region. (d) The merged image of (a) and (b). (e) The subtraction image of (a) and (b). (f) and (g) The amplitude profile plots of lines I and II in panel (d). (red, PAI for water; green, PAI for lipid). (Scale bar: 1 mm.)

can achieve the visualization of more complex tissue structures. The merged image shown in Fig. 10(d) confirms that the distribution of the two kinds of tissue is specific and mapped correctly. Note the high contrast of water content in adipose tissue at 1930 nm; the overlapping in the merged image can be taken as the artifact of water content at 1750 nm. In the merged images, when the water-based signal is taken to be the negative contrast, the lipid contrast is substantially improved as the artifact signals in the regions with high water content are suppressed. In addition, according to the profile plot of lines I and II, we could also find the narrower profile peaks [Fig. 10(f)] and more details [Fig. 10(g)] thanks to the higher contrast of the water PA signal. This phenomenon is caused by the ultrahigh contrast of the excitation light for water and lipids, just as shown in Fig. 5(a). Despite the merged image, the image subtraction is demonstrated for exploring the negative contrast of water content in improving lipid imaging as well [Fig. 10(e)]. By subtracting the signal of water content from the image Fig. 10(a), the image reveals many fine features and distinct boundaries (regions 1, 3, and 4) owing to the suppressed artifact. Meanwhile, the weak signal of adipose tissue in Fig. 10(b) is relatively enhanced (regions 2 and 4). The reason for the enhancement is that the adipose tissue should be located after the thin muscle tissue, and therefore have weak water component and lipid component signals at the same time. Noting the high contrast of the water content to the lipid mentioned above, the enhanced signal is unlikely to be the result of mutual interference between water and lipid signals. All the above improvements benefit from the higher contrast and more details of water PAI at 1930 nm. The result shows the high performance of water content imaging can be beneficial not only to describe the boundary of adipose tissue more distinctly but also to pinpoint the location of the lipid content more precisely.

4 Discussion and Conclusion

The performance of PAI is largely determined by the properties of the excitation laser, including the wavelength as well as its pulse performance. The new HOPE system was devised to provide high-performance pulses for PAI with the output wavelength matching the strong absorption peak of water at 1930 nm. These improvements are reflected by the high SNR of the water PA signal and the enhanced water contrast compared to other chromophores, as well as better penetration depth. Previously, the influence factor of a laser source for PAI was mostly discussed in terms of the excitation wavelength for the chromophores' absorption peak spectrum and the pulse duration for high imaging depth. However, this new HOPE system leverages a higher OSNR and spectrum purity that benefits PAI on low pulse energy required, further expediting high repetition rates for a faster imaging speed.

Additionally, the output wavelength can also be tuned over a wide range. Because the difference between the wavelength of the pump light and the zero-dispersion wavelength of HNLF determines the output center wavelength through the four-wave mixing effect and the different types of doped fiber further determine the cavity gain, the HOPE output consequently can be varied by tuning the pump wavelength and replacing the doped fiber in the cavity. Although this adjustment will somewhat disrupt the pulse after the HNLF regarding the pulse and spectral widths, decreasing the pulse width of EML output through function generator can still compensate for the pulse width broadening. Moreover, the doped fiber can suppress the amplification and resonance at edge wavelengths by selecting the appropriate gain interval. By these means, the new HOPE can easily be adjusted for imaging different chromophores in the NIR window, such as lipids at 1.7 μm.

As to the output power of the new HOPE system, we demonstrate its linear increase with the pump power to the TDFA in low power because the pump laser has low maximum output power, and the pulse energy is enough for follow-up PAI experiments. For higher output power, the new HOPE can be pumped by a high-energy pump laser, or for much higher power requirements, by one or multiple master oscillator power amplifiers (MOPAs).

We also explore the water imaging in the NIR window by the new HOPE. Here, our results not only demonstrated the feasibility of high-sensitivity water PAM in biological systems but also implicated biological and medical applications. Monitoring changes in the water distribution of zebrafish embryos can provide fundamental knowledge of water metabolism in early developmental processes and help identify potential developmental abnormalities. Visualizing water content in liver tumor xenografts can aid in assessing tumor growth, response to therapy, and identifying areas with increased vascular permeability. Mapping fluid distribution in edema can help evaluate the severity of inflammation, tissue injury, and the effectiveness of treatments. Moreover, dual-color PAM for quantitative imaging of lipid and water distribution enables the study of complex biological processes, such as lipid metabolism, tissue remodeling, and the balance between lipid and water content in various diseases. These applications showcase the versatility of the HOPE source in addressing critical biological and medical questions, ultimately highlighting its potential to contribute significantly to the advancement of PAI and its clinical adoption.

From an alternative perspective, water imaging can also help suppress image artifacts, as water exhibits nonnegligible absorption in the NIR window—especially in longer wavelengths—which causes artifact signals in PAI of other chromophores. We demonstrate the water PAI at 1930 nm for not only the positive contrast in water content imaging but also the negative contrast in lipid imaging, which was barely noticed in previous studies. For positive contrast, water content imaging shows high SNR of the water signal as well as enhanced penetration depth, describing the distribution of water content and the tissue with higher water content (e.g., muscle tissue) as well as promising great potential in preclinical and clinical applications (e.g., edema imaging). The introduction of the new HOPE imaging system presents a plethora of opportunities to significantly accelerate advancement in this PAI direction. For negative contrast, water content imaging provides an elegant approach to improve imaging quality (including artifact suppression), show the distinct tissue boundary with low water content, enhance the weak signal of deep tissue, and improve the signal-to-background ratio of the image. Utilizing the negative contrast of water content can potentially drive PAI research for other substances such as the lipid in the NIR window, which has the trade-off between high absorption/deep penetration and strong water interference.

Currently, there is still much room for improvement in relation to the PA image acquisition time. Expediting imaging speed is imperative in preserving the integrity of biosamples, observing faster biological dynamics, and imaging a greater number of samples more efficiently. Although the repetition frequency of the new HOPE was sufficient for rapid image acquisition, we

also admit that the total acquisition time was still too long. This main limitation was due to the stage scanning speed, data collection, and data return speed (using an oscilloscope), rather than the repetition frequency of the new HOPE. Thus, many PA signals excited by light pulses with higher repetition frequencies were missed or not collected. This is the main reason why there was a 5-order of magnitude difference in A-scan and repetition rates. In future work, we plan to employ a faster scanning method and employ a data acquisition card to significantly reduce image acquisition time, thereby showcasing the high repetition rate advantage.

In summary, here we have presented an improved fiber-based OPO, aka the new HOPE, which is characterized by its output of highly stable pulses with a narrow spectral bandwidth and high OSNR at 1930 nm to achieve better water content imaging with high SNR, more elevated penetration depths, and significant contrast. Thanks to the high OSNR and pure spectrum, our PAI system can be achieved with much lower pulse powers, minimizing the sample photodamage risks and realizing a higher-speed PAI. Through this study, the usage of a previously underappreciated optical window at 1930 nm is also highlighted to showcase great potential in water imaging and artifact signal suppression in the NIR window. Furthermore, the HOPE architecture can potentially provide wavelengths in other NIR windows in conjunction with ultrahigh peak power output through combination with a high-power pump or MOPA. Moreover, the new HOPE also exhibits a high dynamic range by lower pulse excitation power and higher emission power, suitable for even more advanced PAI system development. All in all, the current work opens new opportunities for PAI with high-performance laser sources as well as the underexplored optical window at 1930 nm.

5 Appendix: Experimental/Methods

5.1 EML

We chose the EML to generate the modulated optical pulse as the pump for three main advantages. First, the EML only needs to control the driving electrical signal for pulse modulation without setting the bias as the external modulator, which prevents the risks of bias draft and high-intensity noise. These factors further stabilize the optical pulse in the time domain. Second, the tunable extinction ratio of the EML can decrease the ASE noise induced by the TDF gain in the loop. Third, the high switch speed (10 Gbit/s) of the EML is ideal for the application of nanosecond-level pulses, and the EML also eliminates the need for additional modulation devices, reducing system complexity and cost.

5.2 Driven Signal for EML

The electric-driven signal for EML is generated by a functional generator (Liquid Instruments, Moku: Pro) with a low time jitter. The electric impulse signal has a 5 ns pulse width with a 0.5 ns rise/fall edge. The repetition rate of the impulse signal matches the natural resonant frequency of the loop, which is around 187.5 kHz. The modulation depth of the EML is tuned by the bias voltage of the function generator with fixed positive voltage. To further ensure the stability of the modulated pulse, the function generator is synchronized to a rubidium clock (Stanford Research Systems, FS725). Thus, the EML can output a stable rectangle optical pulse.

5.3 Polarization in the Loop

The HNLF (HNLF-SPINE, OFS) used in the setup has a nonlinearity coefficient γ of 15 $W^{-1} \cdot km^{-1}$, dispersion value β_2 of -1.4 ps/(nm · km), and zero dispersion wavelength at 1566 nm. The four-wave mixing process is achieved in the HNLF. During this process, linear polarization contributes to optimal phase-matching conditions, resulting in significant four-wave mixing. To avoid polarization fading of long fiber in the feedback loop, the WDM, circulator, and fiber coil are polarization-maintained. The PC in front of the HNLF is used to fine-tune the slow axis polarization to match the linear polarization for HNLF. In the feedback loop, another PC and an optic polarizer in fiber are used to adjust the polarization state before feeding into the PM coil, which is not shown in Fig. 1. From this, it can stabilize the polarization state of the loop and the best four-wave mixing state to ensure the stable oscillation of the loop.

5.4 Repetition Rate of New HOPE

The repetition rate of new HOPE is equal to the fundamental cavity repetition rate, which is related to the total length of the cavity. The total length of the cavity includes 1.04 km PM coil, 50 m HNLF, and 0.8 m TDF. To match the frequency of the drive signal to the fundamental cavity repetition rate and keep the loop stabilization, a tunable delay line (Luna, VDL-001) is added in the loop to fine-tune the fundamental cavity repetition rate.

5.5 Image Processing

All images were reconstructed offline in MATLAB after oscilloscope sampling. For each image, after performing Hilbert transformation on the waveform of each pixel point data, the maximum values of the transformed data were taken to construct the 2D image. After that, the images were smoothed and pseudo-colored by ImageJ.

5.6 Sample Preparation for Tissue Study

Samples of sliced and bulk bovine were purchased from a local supermarket. The thinly sliced bovine tissue was obtained by cutting frozen beef into approximately 1 mm thick pieces with a slicing device, while the bulk bovine tissues were cut into 1 cm thick pieces. Before imaging, the bovine tissues were further cut smaller with a scalpel to be placed in the chambers and photographed.

5.7 Depth Calculation

The raw data are first transformed into a 3D matrix that contains the PA signal of each pixel. Then the envelope of the signal at each pixel is taken by Hilbert transform to minimize the interference of the artifact. The depth information of each pixel is calculated based on the vertical light proportion in solid (2×108 m/s) and the time scale of the oscilloscope. Finally, the 3D image is rescaled on ImageJ, and the depth is finally calculated by the cross section of the image. For the selection of data points, we chose the data in four edges of the image (10 pixel × 8 pixel) and took the RMS value as the noise floor. The farthest two numerical points in the Y-axis direction greater than 3 times the RMS value are the selected maximum depths.

5.8 Zebrafish Embryo Imaging

The zebrafish embryo was hatched in the laboratory until 48 hpf and then frozen in ice water. Afterward, the embryo was wiped with dust-free paper to remove moisture from its surface and then immersed in silicone oil for PAI. The zebrafish developmental stage at 48 hpf does not exceed the limits for unprotected developmental stages (120 hpf) set by animal welfare legislation.[54]

5.9 Orthotopic Liver Tumor Xenograft Model and Ear Edema Model

Male immunodeficient SCID mice at about 4 to 5 weeks old were obtained from the Centre for Comparative Medicine Research, The University of Hong Kong. The use of mice to develop orthotopic liver tumor xenografts was approved by the Committee on the Use of Live Animals in Teaching and Research (CULATR), The University of Hong Kong, Hong Kong (approval number: 5395-20). The animals were acclimated for one week in a pathogen-free environment prior to being utilized in this study. The protocol to develop orthotopic tumor xenografts was followed according to the previous report.[55] Briefly, a total of 5×10^6 MHCC97-L cells were resuspended in 100 μL phosphate-buffered saline and injected orthotopically into the left liver lobe of each mouse. Orthotopic tumors were allowed to grow for three to four weeks. At the end of the experiments, the mice were all euthanized and their fresh tumor xenografts were collected and imaged.

The ear edema model was performed as previously described.[56] Twenty-μL dimethylbenzene solution was applied evenly on the surface of both sides of the mouse's right ear to induce edema. After 30 min, both left and right ears were taken off and hairs were removed before imaging.

Disclosures

The authors declare no conflicts of interest.

Code and Data Availability

The data sets used and/or analyzed during the current study are available from the corresponding author upon reasonable request.

Author Contributions

H.T., Y.T., J.S., M.L., C. J., and K.K.W. planned the experiments. Y.T. developed the study on the new HOPE system. H.T. and Y.T. developed the new HOPE system and the PA microscopy. H.T. and M.L. developed the computer program for PAI and data processing. H.T., Y.T., and N.S. performed the PAI experiments. B.L. performed the animal experiment. H.T. carried out the data analysis. H.T., Y.T., M.L., N.S., B.L., C. J., and K.K.W. wrote the manuscript. K.K.W, K.K.T., and N.P.L supervised the project. All authors discussed the results and approved the final manuscript.

Acknowledgments

This work was supported by the Research Grants Council of the Hong Kong Special Administrative Region (SAR) of China (Grant Nos. HKU 17210522, HKU C7074-21G, HKU 17205321, and HKU 17200219), ITF MHKJFS Projects (Grant Nos. MHP/073/20 and MHP/057/21), and the Health@InnoHK Program of the Innovation and Technology Commission of the Hong Kong SAR Government.

References

1. P. Ball, "Water as an active constituent in cell biology," *Chem. Rev.* **108**(1), 74–108 (2008).
2. M. Chaplin, "Do we underestimate the importance of water in cell biology," *Nat. Rev. Mol. Cell Biol.* **7**(11), 861–866 (2006).
3. L. Shi et al., "Optical imaging of metabolic dynamics in animals," *Nat. Commun.* **9**(1), 1–17 (2018).
4. E. Alonso-Ortiz, I. R. Levesque, and G. B. Pike, "MRI-based myelin water imaging: a technical review," *Magn. Reson. Med.* **73**(1), 70–81 (2015).
5. M. Maurer and C. Oostenbrink, "Water in protein hydration and ligand recognition," *J. Mol. Recognit.* **32**(12), e2810 (2019).
6. Z. Xu, L. V. Wang, and Q. Zhu, "In vivo photoacoustic tomography of mouse cerebral edema induced by cold injury," *J. Biomed. Opt.* **16**(6), 066020 (2011).
7. R. G. Steen, "Edema and tumor perfusion: characterization by quantitative 1H MR imaging," *Amer. J. Roentgenol.* **158**(2), 259–264 (1992).
8. C.-S. Liao et al., "Microsecond scale vibrational spectroscopic imaging by multiplex stimulated Raman scattering microscopy," *Light: Sci. Appl.* **4**(3), e265 (2015).
9. C. Rao, N. C. Verma, and C. K. Nandi, "Unveiling the hydrogen bonding network of intracellular water by fluorescence lifetime imaging microscopy," *J. Phys. Chem. C* **123**(4), 2673–2677 (2019).
10. K. Kimura et al., "Visualizing water molecule distribution by atomic force microscopy," *J. Chem. Phys.* **132**(19), 194705 (2010).
11. L. V. Wang and J. Yao, "A practical guide to photoacoustic tomography in the life sciences," *Nat. Methods* **13**(8), 627–638 (2016).
12. J. Yao and L. V. Wang, "Photoacoustic microscopy," *Laser Photonics Rev.* **7**(5), 758–778 (2013).
13. J. Hui et al., "Bond-selective photoacoustic imaging by converting molecular vibration into acoustic waves," *Photoacoustics* **4**(1), 11–21 (2016).
14. S. Wang et al., "Recent advances in photoacoustic imaging for deep-tissue biomedical applications," *Theranostics* **6**(13), 2394 (2016).
15. W. Chen, C. Tao, and X. Liu, "Artifact-free imaging through a bone-like layer by using an ultrasonic-guided photoacoustic microscopy," *Opt. Lett.* **44**(5), 1273–1276 (2019).
16. Z. Xu, C. Li, and L. V. Wang, "Photoacoustic tomography of water in phantoms and tissue," *J. Biomed. Opt.* **15**(3), 036019 (2010).
17. J. Li et al., "Time-domain terahertz optoacoustics: manipulable water sensing and dampening," *Adv. Photonics* **3**(2), 026003 (2021).
18. J. A. Curcio and C. C. Petty, "The near-infrared absorption spectrum of liquid water," *JOSA* **41**(5), 302–304 (1951).
19. J.-X. Cheng, "New 'HOPE' laser for photoacoustic imaging of water," *Light: Sci. Appl.* **11**(1), 1–2 (2022).
20. P. K. Upputuri and M. Pramanik, "Photoacoustic imaging in the second near-infrared window: a review," *J. Biomed. Opt.* **24**(4), 040901 (2019).
21. L. A. Sordillo et al., "Advances in medical applications using SWIR light in the wavelength range from 1000 to 2500 nm," *Proc. SPIE* **10873**, 108730T (2019).
22. W. M. Irvine and J. B. Pollack, "Infrared optical properties of water and ice spheres," *Icarus* **8**(1-3), 324–360 (1968).
23. J. Swiderski, M. Michalska, and G. Maze, "Mid-IR supercontinuum generation in a ZBLAN fiber pumped by a gain-switched mode-locked Tm-doped fiber laser and amplifier system," *Opt. Express* **21**(7), 7851–7857 (2013).
24. W. Ma et al., "1.9 μm square-wave passively Q-witched mode-locked fiber laser," *Opt. Express* **26**(10), 12514–12521 (2018).
25. G. De Valcarcel et al., "Transverse patterns in degenerate optical parametric oscillation and degenerate four-wave mixing," *Phys. Rev. A* **54**(2), 1609 (1996).
26. G. Wong et al., "High-conversion-efficiency widely-tunable all-fiber optical parametric oscillator," *Opt. Express* **15**(6), 2947–2952 (2007).

27. C. Li et al., "High-power widely tunable all-fiber thulium-assisted optical parametric oscillator at SWIR band," *Opt. Lett.* **41**(22), 5258–5261 (2016).
28. H.-W. Wang et al., "Label-free bond-selective imaging by listening to vibrationally excited molecules," *Phys. Rev. Lett.* **106**(23), 238106 (2011).
29. R. Cao et al., "Multispectral photoacoustic microscopy based on an optical–acoustic objective," *Photoacoustics* **3**(2), 55–59 (2015).
30. P. Wang et al., "Bond-selective imaging of deep tissue through the optical window between 1600 and 1850 nm," *J. Biophotonics* **5**(1), 25–32 (2012).
31. G. Bi et al., "Compact, 2.95-GHz repetition-rate femtosecond optical parametric oscillator with tunable pulse repetition frequency," *Opt. Commun.* **500**, 127339 (2021).
32. H. K. Choi, *Long-Wavelength Infrared Semiconductor Lasers*, Wiley Online Library (2004).
33. J. Shi et al., "Hybrid optical parametrically-oscillating emitter at 1930 nm for volumetric photoacoustic imaging of water content," *eLight* **2**(1), 1–7 (2022).
34. H. Tang et al., "A novel fiber optical parametric oscillator for high-contrast and high-speed photoacoustic imaging of water," in *TENCON 2022-2022 IEEE Region 10 Conf. (TENCON)*, pp. 1–4 (2022).
35. I. Begleris and P. Horak, "Efficiency and intensity noise of an all-fiber optical parametric oscillator," *J. Opt. Soc. Amer. B* **36**(3), 551–558 (2019).
36. S. Brosnan and R. Byer, "Optical parametric oscillator threshold and linewidth studies," *IEEE J. Quantum Electron.* **15**(6), 415–431 (1979).
37. M. E. Marhic, *Fiber Optical Parametric Amplifiers, Oscillators and Related Devices*, Cambridge University (2008).
38. E. Zlobina and S. Kablukov, "Fiber optical parametric oscillators," *Optoelectron. Instrum. Data Process.* **49**(4), 363–382 (2013).
39. G. P. Agrawal, *Lightwave Technology: Telecommunication Systems*, John Wiley (2005).
40. N. Englebert et al., "Parametrically driven Kerr cavity solitons," *Nat. Photonics* **15**(11), 857–861 (2021).
41. H. Høgset et al., "In vivo biomolecular imaging of zebrafish embryos using confocal Raman spectroscopy," *Nat. Commun.* **11**(1), 6172 (2020).
42. M. Hagedorn et al., "Water distribution and permeability of zebrafish embryos, Brachydanio rerio," *J. Exp. Zool.* **278**(6), 356–371 (1997).
43. T. Zhang, D. M. Rawson, and G. J. Morris, "Cryopreservation of pre-hatch embryos of zebrafish (Brachydanio rerio)," *Aquatic Living Resour.* **6**(2), 145–153 (1993).
44. N. L. Henry and D. F. Hayes, "Cancer biomarkers," *Mol. Oncol.* **6**(2), 140–146 (2012).
45. M.-F. Penet et al., "Water and collagen content are high in pancreatic cancer: implications for quantitative metabolic imaging," *Front. Oncol.* **10**, 599204 (2021).
46. J. Fu and H. Wang, "Precision diagnosis and treatment of liver cancer in China," *Cancer Lett.* **412**, 283–288 (2018).
47. S. G. Rockson, "The diagnosis of edema and its pathogenesis," in *Lymphedema*, BB. Lee, S. Rockson, and J. Bergan, Eds., pp. 221–228, Springer International Publishing, Cham, Switzerland (2018).
48. R. A. Fishman, "Brain edema," *New Engl. J. Med.* **293**(14), 706–711 (1975).
49. H. K. Kim, S. Y. Namgoong, and H. P. Kim, "Antiinflammatory activity of flavonoids: mouse-ear edema inhibition," *Arch. Pharm. Res.* **16**, 18–24 (1993).
50. K. Murakami et al., "Cold injury in mice: a model to study mechanisms of brain edema and neuronal apoptosis," *Progr. Neurobiol.* **57**(3), 289–299 (1999).
51. P. Wang et al., "Mapping lipid and collagen by multispectral photoacoustic imaging of chemical bond vibration," *J. Biomed. Opt.* **21**(9), 096010 (2012).
52. L. Li et al., "Label-free photoacoustic tomography of whole mouse brain structures ex vivo," *Neurophotonics* **3**(3), 035001 (2016).
53. C. Li et al., "High-energy all-fiber gain-switched thulium-doped fiber laser for volumetric photoacoustic imaging of lipids," *Photonics Res.* **8**(2), 160–164 (2020).
54. C. B. Kimmel et al., "Stages of embryonic development of the zebrafish," *Dev. Dynam.* **203**(3), 253–310 (1995).
55. P. Dong et al., "HFE promotes mitotic cell division through recruitment of cytokinetic abscission machinery in hepatocellular carcinoma," *Oncogene* **41**(36), 4185–4199 (2022).
56. D. Dong et al., "Sarsasapogenin-AA13 inhibits LPS-induced inflammatory responses in macrophage cells in vitro and relieves dimethylbenzene-induced ear edema in mice," *Acta Pharmacol. Sin.* **38**(5), 699–709 (2017).
57. Y. Liu, C. Zhang, and L. V. Wang, "Effects of light scattering on optical-resolution photoacoustic microscopy," *J. Biomed. Opt.* **17**(12), 126014 (2012).
58. L. Y. Shi et al., "Transmission in near-infrared optical windows for deep brain imaging," *J. Biophotonics* **9**(1), 38–43 (2015).
59. T. Y. Wang and C. Xu, "Three-photon neuronal imaging in deep mouse brain," *Optica* **7**(8), 947–960 (2020).

Biographies of the authors are not available.